Brain Structure and Function (2019) 224:2567–2576
https://doi.org/10.1007/s00429-019-01908-7

SHORT COMMUNICATION

Ensemble encoding of action speed by striatal fast-spiking interneurons

Bradley M. Roberts[1] · Michael G. White[1] · Mary H. Patton[1] · Rong Chen[2] · Brian N. Mathur[1]

Received: 27 December 2018 / Accepted: 8 June 2019 / Published online: 26 June 2019

Abstract

Striatal fast-spiking interneurons (FSIs) potently inhibit the output neurons of the striatum and, as such, powerfully modulate action learning. Through electrical synaptic coupling, FSIs are theorized to temporally coordinate their activity. This has important implications for their ability to temporally summate inhibition on downstream striatal projection neurons. While some in vivo single-unit electrophysiological recordings of putative FSIs support coordinated firing, others do not. Moreover, it is unclear as to what aspect of action FSIs encode. To address this, we used in vivo calcium imaging of genetically identified FSIs in freely moving mice and applied machine learning analyses to decipher the relationship between FSI activity and movement. We report that FSIs exhibit ensemble activity that encodes the speed of action sub-components, including ambulation and head movements. These results suggest FSI population dynamics fit within a Hebbian model for ensemble inhibition of striatal output guiding action.

Keywords GABA · Inhibition · Basal ganglia · Striatum · Calcium imaging · Endoscope · Ensemble · Kinematics

Introduction

The dorsal striatum is the input nucleus for cortical processing by the basal ganglia and, as such, is critical for voluntary action learning and control. The principal neuron type of the striatum is the medium spiny projection neuron (MSN), which receives powerful feedforward inhibition from striatal parvalbumin-expressing fast-spiking interneurons (FSIs; Koos et al. 2004; Tepper et al. 2004). FSIs are critical for habit (O'Hare et al. 2017) and egocentric learning strategies (Owen et al. 2018). Post-mortem examinations of brains from individuals with a history of the motor tic disorder Tourette syndrome reveal a 50% decrease in FSI numbers (Kalanithi et al. 2005; Kataoka et al. 2010). Despite the critical role that FSIs play in action control, it remains unclear how FSI encoding of action compares to MSNs, which encode complex features of actions (Jin and Costa 2010; Graybiel 1998; Barnes et al. 2011; Klaus et al. 2017; London et al. 2018) and kinematic properties of movement (Yttri and Dudman 2016; Barbera et al. 2016).

Computational models of FSI population activity suggest that FSI electrical coupling enables population-wide synchrony (Hjorth et al. 2009; Zhang et al. 2014). However, in vivo single-unit recordings of putative FSIs suggest that FSIs fire idiosyncratically (Berke 2008), while other data provide evidence that FSIs fire in a coordinated fashion (Bakhurin et al. 2016). A possible explanation for this discrepancy could be the organization of FSIs into functional ensembles. FSIs diffusely populate the striatum and represent less than 3% of all striatal neurons (Tepper et al. 2010). Thus, using electrophysiological approaches, it is very difficult to assess: (1) whether ensemble activity exists and; (2) what aspect of actions FSI ensembles may encode. To address this, we apply in vivo calcium (Ca^{2+}) imaging to visualize activity-dependent Ca^{2+} signals in freely behaving adult mice. We report that FSIs functionally organize as ensembles that encode the speed of distinct movement sub-components.

Bradley M. Roberts and Michael G. White have contributed equally to this work.

✉ Brian N. Mathur
BMathur@som.umaryland.edu

[1] Department of Pharmacology, University of Maryland School of Medicine, HSF III 9179, 670 West Baltimore Street, Baltimore, MD 21201, USA

[2] Department of Diagnostic Radiology and Nuclear Medicine, University of Maryland School of Medicine, Baltimore, MD, USA

Materials and methods

Animals

All procedures were performed in accordance with the United States Public Health Service Guide for Care and Use of Laboratory Animals and were approved by the Institutional Animal Care and Use Committee at the University of Maryland Baltimore. Mice were housed with littermates (2–5 per cage) under a 12-h light/dark cycle (lights on at 0700 h, off at 1900 h) with *ad libitum* access to food and water. A total of 12 *Pvalb-Cre* (Tanahira et al. 2009) female and male transgenic mice (C57BL/6 J background) were used for this study. Mice were 6–36 weeks old.

Stereotaxic surgery and viral vectors

6–10-week-old mice were anesthetized with isoflurane and placed into a stereotaxic frame. For slice experiments, adeno-associated viral (AAV) vectors (UPenn Vector Core) were used for *Cre*-dependent expression of the genetically encoded Ca^{2+} indicator GCaMP6f (AAV5-Syn-Flex-GCaMP6f-WPRE-SV40) in the dorsal striatum of *Pvalb-Cre* mice: + 0.8 mm anterior/posterior (AP) from bregma, ± 1.8 mm medial/lateral (ML) from midline, and − 2.2 mm dorsal/ventral (DV). Four weeks after surgery, the slice experiments were performed. For in vivo experiments, injections of the GCaMP6f viral construct were performed at a 30° angle from the DV axis and caudally from bregma at: − 0.9 mm AP from bregma, ± 1.8 mm ML from midline, and − 3.46 mm DV from brain surface. 500 nL of virus was injected at a rate of 15–25 nL/min with an infusion time of 7–10 min.

In vivo Ca^{2+} imaging of FSIs

An imaging cannula (Doric) containing a graded-index (GRIN) lens (0.5-mm diameter, 3.13-mm length) was stereotaxically implanted unilaterally into the dorsal striatum (+ 0.8 mm AP from bregma, ± 1.8 mm ML from midline, − 2.0 mm DV from top of brain) 3–4 weeks following GCaMP6f viral injections. Imaging canulae were affixed to the skull with Titan Bond (Horizon Dental) and dental cement. Following 3–4 weeks of surgical recovery, a miniaturized epifluorescence microscope (Doric Lenses) was attached to the implanted cannula, and mice were habituated to this procedure over 10 sessions across 5 days. After habituation, Ca^{2+} imaging data were acquired using the Doric Microscope Controller 2.1 software at 10 Hz under 1.2–1.7 mW blue light (435 nm) excitation. Frames were 630 × 630 pixels (~ 350 × 350 µm). FSIs were imaged during free ambulatory behavior in an acrylic chamber (50 cm × 30 cm) and video monitored from above. The position of the center of mass of each mouse was tracked using Ethovision XT software (Noldus). A smoothing algorithm was applied to all video tracks before analysis to reduce system noise (locally weighted scatterplot smoothing based on ten points before or after each data point performed in Ethovision XT). Imaging sessions lasted 2.5 min.

Image processing

Image pre-processing was performed with the Doric Image Analyzer software 1.0 (Guizar-Sicairos et al. 2008; Doric Lenses) and included image realignment to correct for motion-related artifacts and signal background subtraction. Aligned and background-subtracted images were processed in MATLAB R2013a (MathWorks) to extract denoised $\Delta F/F$ activity of manually selected FSIs according to previously established methods (Pnevmatikakis et al. 2016). No spatial or temporal down-sampling was applied. Extracted denoised $\Delta F/F$ signals were used for cross-correlations and machine learning analyses.

Analysis of movement

All movements were scored as either an isolated head movement, isolated ambulation, or a combined head movement and ambulation. After manual scoring, the speed data were recoded into two time series corresponding to either head movement or ambulation epochs. Recoding was done so that the new head movement and ambulation time series maintained the same length as the original speed time series. For the head movement time series, ambulation events were coded as a speed of zero and vice versa. Any movements comprised of both head movements and ambulation were coded as zero.

Acute slice electrophysiology

Mouse striatal slices were prepared according to our previously published methods (Patton et al. 2016). All whole-cell experiments were recorded using borosilicate glass pipettes with resistance of 2–7 MΩ. Cells were current clamped using a Multi Clamp 700B amplifier (Molecular Devices) and Clampex 10.4.1.4 software (Molecular Devices) was used for data acquisition. All recordings were filtered at 2 kHz and digitized at 10 kHz. Micropipettes were filled with a K-Gluconate internal solution (in mM: 126 K-Gluconate, 4 KCl, 10 HEPES, 4 ATP-Mg, 0.3 GTP-Na, and 10 Phosphocreatine; osmolarity ranging from 290 to 295 mOsm; pH 7.3). FSIs were recorded at 40× under blue light (470 nm) exposure with an optiMOS sCMOS camera (Q Imaging) at 10 frames per second. Denoised $\Delta F/F$ activity was extracted

during voltage steps as described above. Linear regressions were performed between the max $\Delta F/F$ value and number of spikes generated during the voltage step for each cell.

Immunohistochemistry

Immunohistochemistry was performed as per our previously published methods (White et al. 2017). Primary antibodies used included goat anti-PV (1:5000, Swant PVG-214) and chicken anti-GFP (1:2000, Abcam ab13970). Secondary antibodies used were Alexa Fluor® 488 (donkey anti-goat, donkey anti-chicken, 1:1000, Jackson ImmunoResearch).

Predictive modeling

A generalized boosted model (GBM) was used for neural decoding (Friedman 2001, 2002). GBM produces an ensemble of prediction models, which are built in a stage-wise fashion. Here, GBM was implemented using an R machine learning package: caret (Kuhn 2008). Prediction performance is evaluated based on tenfold cross-validation (Duda et al. 2001). For cross-validation, we divided the dataset into ten blocks; we used 9 blocks to train a predictive model and used 1 block to test the model. The prediction performance was quantified by Pearson's product-moment correlation coefficient.

Neural decoding was formulated by constructing a predictive model f: $b \rightarrow Y$, where b is Ca^{2+} signals, and Y is the behavior variable (e.g., speed). Training a model from a training dataset $D = [(b_1, y_1), \ldots, (b_k, y_k), \ldots (b_N, y_N)]$ is to minimize a desired objective function, where (b_k, y_k) is the kth case in the training dataset. For continuous behavior variables, a widely used objective function is mean square errors. The procedure of GBM is as follows: GBM initializes $f(\boldsymbol{b})$ by a constant, then GBM iteratively performs the following steps: (1) compute the negative gradient; (2) fit a regression model $g(B)$; (3) choose a gradient descent step size ρ, and; (4) update $f(b)$ as $f(b) \leftarrow f(b) + \rho g(B)$.

Statistical analyses

Cross-correlations of $\Delta F/F$ signals were calculated pairwise for all identified FSIs in each mouse. Additionally, cross-correlations of $\Delta F/F$ signal and speed during ambulation were calculated for all FSIs in each mouse. A Fisher's z transformation was applied to maximal cross-correlation coefficients within a ± 500 ms time lag for in vivo recordings. Transformed coefficients were averaged for all FSI–FSI and FSI–speed cross-correlations within a mouse before performing one-sample t-tests to determine significance at the group level. To minimize false-positive cross-correlations, a threshold of $p < 0.001$ was used.

Results

Coordinated FSI activity-dependent Ca^{2+} transients in vivo encode movement speed

To first determine if Ca^{2+}-dependent fluorescence changes of GCaMP6f capture the full dynamic range of firing of striatal FSIs, we measured GCaMP6f fluorescence changes across a range of striatal FSI firing rates in acute striatal slices (Fig. 1a). FSIs were targeted for whole-cell patch clamp recordings in current clamp configuration using GCaMP6f fluorescence. We previously confirmed that this *Pvalb-Cre* line selectively expresses Cre in striatal FSIs (Mathur et al. 2013). Baseline fluorescence was defined as that of the non-firing state, which FSIs exhibit in the acute slice preparation in the absence of current injection. A series of progressively larger current injections were given to induce FSI firing while measuring GCaMP6f fluorescence. We observed strong correlations between the maximum magnitude of $\Delta F/F$ signals and firing rate (Fig. 1a; average $r = 0.99$, $n = 12$ cells).

FSIs were next imaged in vivo microendoscopically. Representative implantation of GRIN lens and GCaMP6f expression is shown in Fig. 1b. $\Delta F/F$ signals from Ca^{2+} transients from manually identified FSIs during free movement in an open field were extracted (Fig. 1c). Cross-correlating FSI $\Delta F/F$ signals for all possible FSI pairs within each animal revealed that FSI–FSI activity was significantly correlated (Fig. 1d; average $r_{max} = 0.42 \pm 0.08$, $n = 136$ FSI pairs from 9 mice; average Fisher z transformation $= 0.51 \pm 0.1$, $n = 9$ mice, $t = 3.8$, $p = 0.005$, one-sample t test). The distribution of Fisher z transformation values calculated from the FSI–FSI cross-correlations deviated from a normal distribution (Fig. 1d; Shapiro–Wilk normality test, $p = 0.04$).

Cross-correlating FSI $\Delta F/F$ signals with movement speed revealed a positive cross-correlation (Fig. 1e; average $r_{max} = 0.40 \pm 0.06$, $n = 49$ cells from 9 mice; average Fisher z transformation $= 0.44 \pm 0.08$, $n = 9$ mice, $p = 0.0004$, one-sample t test). The distribution of Fisher z transformation values calculated from the FSI–speed cross-correlations did not deviate from a normal distribution (Fig. 1e; Shapiro–Wilk normality test, $p = 0.12$). In addition, we found that FSI $\Delta F/F$ signals were consistently elevated around the peak speed of movements relative to bouts of inactivity (Fig. 1f; mean $\Delta F/F$ for peak movement $= 0.69 \pm 0.09$, for no movement $= 0.11 \pm 0.04$, $t = 7.54$, $n = 9$ animals, $p < 0.005$, paired t test).

FSI ensemble encoding of movement sub-components

The heterogeneity of the observed FSI–FSI cross-correlations (Fig. 1d) suggests that FSIs may be functionally organized as ensembles. To examine the relationship between

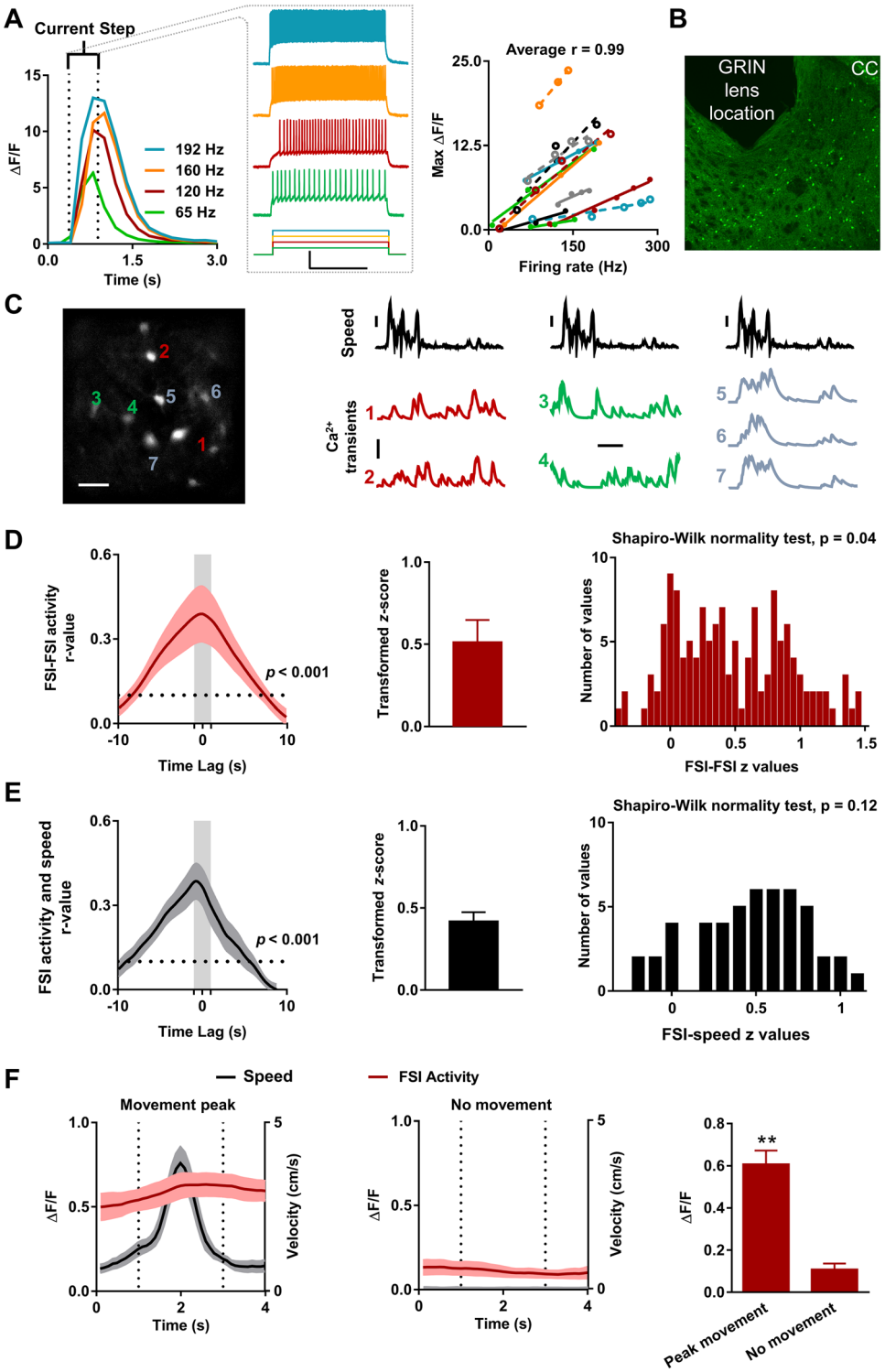

movement subcomponents and potential ensemble activity, we cross-correlated FSI $\Delta F/F$ signals with head and ambulatory movement, respectively (Fig. 2a, b). We found that some FSIs were more positively correlated with ambulation speed than with head movement speed (Fig. 2a) and vice versa (Fig. 2b). A stringent threshold was applied to differentiate these FSI subtypes ($p < 0.001$) to minimize any Type I error. Other FSIs were positively correlated with both types of movement speed (ambulation/head), and another subset of FSIs were not correlated with either type of movement (stochastic). A breakdown of all the different identified subtypes of FSIs is shown in Fig. 2c.

◂**Fig. 1** Coordinated activity of fast-spiking interneurons (FSIs) in vivo correlates with movement speed. **a** Left: representative Δ*F*/*F* signals from a striatal FSI expressing GCaMP6f along with representative action potential firing in FSIs recorded using whole-cell patch clamp recordings in current clamp configuration. Increasing firing frequencies were induced by progressively larger current steps (translating to depolarization increments of 10 mV). Right: relationship between firing rate and maximum Δ*F*/*F* signal plotted per cell. The average within cell *r* was 0.99. Scale bars: 30 mV (vertical) and 125 ms (horizontal). **b** Immunostaining of GCaMP6f and the placement of the gradient refractive index lens (GRIN lens) in the dorsal striatum. *CC* corpus callosum. **c** Left: representative image of striatal FSIs expressing GCaMP6f in vivo. The colored numbers correspond to the Ca2 + transients in these neurons at right. Scale bar: 50 µm. Right: Speed trace for one representative animal (black) and GCaMP6f traces for FSIs demonstrating pairs of FSIs have similar firing patterns (cells 1 and 2; cells 3 and 4; cells 5, 6 and 7). Scale bars: 4 cm/s, 10% Δ*F*/*F*, 10 s. **d** Left: cross-correlogram of Δ*F*/*F* signal from FSI pairs shows a significant coordination of FSI–FSI Δ*F*/*F* signals (mean ± SEM, shaded region). Dotted line represents level of significance ($p < 0.001$). Center: Average Fisher *z* transformation of maximal FSI–FSI cross-correlation *r* values across mice. Right: distribution of fisher *z* transformation values significantly deviated from a normal distribution. **e** Left: cross-correlogram of Δ*F*/*F* signal to speed (FSI–speed) shows a significant correlation of FSI Δ*F*/*F* signals and speed (mean ± SEM, shaded region). Dotted line represents level of significance ($p < 0.001$). Center: average fisher *z* transformation of maximal FSI–speed cross-correlation *r* values across mice. Right: the distribution of fisher *z* transformation values did not deviate from a normal distribution. **f** Average FSI Δ*F*/*F* signal across mice (red traces) was examined within 2-s epochs (dotted lines) of two mobility states: around local speed peaks (gray trace; left) and inactive periods (gray trace, center). Right: average FSI Δ*F*/*F* signal was significantly greater around speed peaks relative to periods of inactivity. $^{**}p < 0.005$

The average Fisher *z* transformation of FSI Δ*F*/*F* cross-correlations to overall speed, ambulation speed, and head movement speed for each FSI subtype is shown in Fig. 2d–g. For the so-called ambulation FSIs, the average cross-correlation of Δ*F*/*F* signal and ambulation speed was significantly greater than the average cross-correlation of Δ*F*/*F* signal and head movement speed (Fig. 2d; average Fisher *z* transformation for ambulation FSIs and ambulation speed = 0.61 ± 0.04, and for ambulation FSIs and head movement speed = 0.009 ± 0.04, $t = 10.1$ $p < 0.0001$, $n = 27$ FSIs, paired *t* test). The reverse was true for head FSIs, as the average cross-correlation of Δ*F*/*F* signal from head FSIs and head speed was greater than the average cross-correlation of Δ*F*/*F* signal and ambulation speed (Fig. 2e; average Fisher *z* transformation for head FSIs and head speed = 0.40 ± 0.07, and for head FSIs and ambulation speed = 0.13 ± 0.08, $t = 12.2$, $p < 0.0001$, $n = 7$ FSIs, paired *t* test). No difference was observed between the average cross-correlations of Δ*F*/*F* signal and ambulation speed or head movement speed for ambulation/head FSIs (Fig. 2f; average Fisher *z* transformation for ambulation/head FSIs and ambulation speed = 0.40 ± 0.04, and for ambulation/head FSIs and head movement speed = 0.36 ± 0.05, $t = 0.68$ $p = 0.51$, $n = 9$ FSIs, paired *t* test), or stochastic FSIs, which did not have any significant cross-correlation with any observed aspect of movement (Fig. 2g; average Fisher *z* transformation for stochastic FSIs and ambulation speed = − 0.06 ± 0.05, and for stochastic FSIs and head movement speed = 0.04 ± 0.02, $t = 1.5$ $p = 0.19$, $n = 6$ FSIs, paired *t* test).

The average cross-correlation of Δ*F*/*F* signal from ambulation FSIs and overall speed did not differ from the average cross-correlation of Δ*F*/*F* signal and ambulation speed (Fig. 2d; average Fisher *z* transformation for ambulation FSIs and speed = 0.68 ± 0.05; $t = 0.59$ $p = 0.56$, $n = 27$ FSIs, paired *t* test), nor did the average cross-correlation of Δ*F*/*F* signal from head FSIs and overall speed significantly differ from the average cross-correlation of Δ*F*/*F* signal and head speed (Fig. 2e; average Fisher *z* transformation for head FSIs and speed = 0.27 ± 0.12; $t = 2.13$ $p = 0.08$, $n = 7$ FSIs, paired *t* test). The cross-correlation with overall speed was greater than average cross-correlations to ambulation speed or head movement speed alone (Fig. 2f; average Fisher *z* transformation for ambulation/head FSIs and speed = 0.49 ± 0.06; ambulation speed vs. speed, $t = 2.41$ $p = 0.04$, $n = 9$ FSIs, paired *t* test; head movement speed vs. speed, $t = 2.59$ $p = 0.03$, $n = 9$ FSIs, paired *t* test).

We next examined the ambulation FSI–FSI cross-correlations from each mouse and compared this to cross-correlations of ambulation FSIs with the other FSI subtypes (Fig. 2h). We only compared ambulation FSIs because these were the most prominent subtype, and thus, there were sufficient numbers of ambulation FSIs in each mouse to allow for comparisons of FSI–FSI coordination to all other FSI subtypes. Cross-correlations among ambulation FSIs were greater than cross-correlations of ambulation FSIs to both head FSIs (Fig. 2h; average Fisher *z* transformation for ambulation–ambulation FSI cross-correlations = 0.71 ± 0.06, 44 pairs, and for ambulation–head FSI cross-correlations = 0.33 ± 0.07, 40 pairs, $t = 3.88$, $p = 0.0003$, unpaired *t* test) and stochastic FSIs (Fig. 2h; average Fisher *z* transformation for ambulation–stochastic FSI cross-correlations = 0.03 ± 0.03, 26 pairs, $t = 8.79$, $p < 0.0001$, unpaired *t* test). In contrast, this difference was not observed for cross-correlation of ambulation FSIs to ambulation/head FSIs (Fig. 2h; average Fisher *z* transformation for ambulation–ambulation/head FSI cross-correlations = 0.68 ± 0.07, 25 pairs, $t = 0.27$, $p < 0.79$, unpaired *t* test).

Predictive modeling of speed

To test if FSI ensembles encode movement speed, we trained generalized boosted models (GBM) (Friedman 2001, 2002) using FSI Δ*F*/*F* signals to predict the speed for each mouse (Fig. 3a). Movement speed was significantly predicted from a minimum of 3 FSI Δ*F*/*F* signals (Fig. 3b, $r = 0.95 \pm 0.02$, Fisher $z = 1.89 \pm 0.15$, $t = 12.94$,

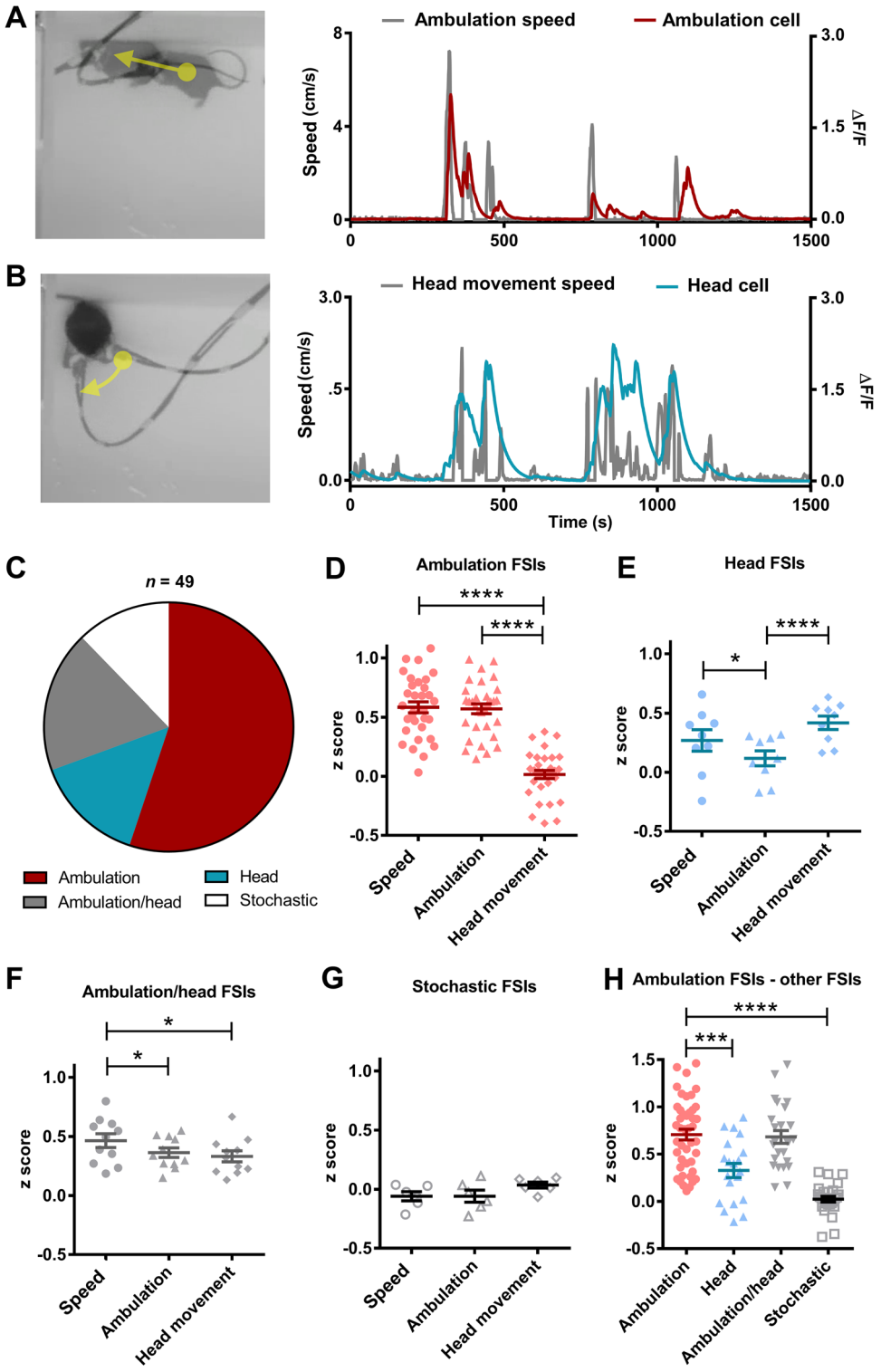

$n = 9$, $p < 0.0001$, one-sample t test). We performed the same GBM analysis using 10 different permutations of shuffled FSI $\Delta F/F$ time series to predict speed and found the mean root mean square error (RMSE) across the ten permutations. For all mice, ensemble FSI activity (Fig. 3c, red bars, average RMSE of ensemble composite FSI activity $= 0.39 \pm 0.006$, $F = 29.2$, $p = 0.0004$, $n = 9$ mice, One-way RM ANOVA) had a greater RMSE in the GBM prediction of speed than using: (1) shuffled FSI data (Fig. 3c, light gray bars, average RMSE of randomized FSI activity $= 1.50 \pm 0.22$, $p = 0.0007$, Dunnett's multiple comparison test); (2) individual FSI data as a

◂**Fig. 2** Ensembles of FSIs encode distinct movements. **a** Left: example of an ambulatory movement. Right: example traces illustrating the relationship between $\Delta F/F$ signal from a striatal FSI preferentially responding to ambulation speed (red) and ambulation speed isolated from the overall speed signal (gray). **b** Left: example of a head movement from the same mouse shown in **a**. Right: example traces illustrating the relationship between $\Delta F/F$ signal from a striatal FSI preferentially responding to head movement speed (blue) and head movement speed isolated from the overall speed signal (gray). **c** The breakdown of striatal FSIs for which $\Delta F/F$ signal preferentially encoded ambulation (ambulation) or head movements (head), as well as FSIs that encoded both ambulation and head movements equally (ambulation/head) or FSIs that did not encode either ambulation or head movement (stochastic). **d** For ambulation FSIs, the cross-correlation between $\Delta F/F$ signal and isolated ambulation speed, as well as overall speed, was greater than the cross-correlation to head movement speed. $^{****}p < 0.0001$. **e** For head FSIs, the cross-correlation between $\Delta F/F$ signal and isolated head movement speed was greater than the cross-correlation to ambulation speed. In addition, for these FSIs the cross-correlation of $\Delta F/F$ signal to overall speed was greater than to ambulation speed. $^{*}p < 0.05$, $^{****}p < 0.0001$. **f** For ambulation/head FSIs, the cross-correlation between $\Delta F/F$ signal and overall speed was greater than the cross-correlation to ambulation speed and to head movement speed. $^{*}p < 0.05$. **g** For stochastic FSIs, cross-correlations between $\Delta F/F$ signals and overall speed, ambulation speed, and head movement speed did not differ. **h** FSI–FSI cross-correlations of $\Delta F/F$ signals were significantly greater between ambulation FSIs and other ambulation FSIs (ambulation–ambulation) compared to ambulation–head and ambulation–stochastic cross-correlations; whereas ambulation–ambulation and ambulation–ambulation/head cross-correlations were not different. $^{***}p < 0.001$, $^{****}p < 0.0001$

predictor and taking the mean of the resulting RMSEs (Fig. 3c, white bars, average RMSE of individual FSI activity = 1.36 ± 0.22, $p = 0.002$, Dunnett's multiple comparison test) or; (3) or the average activity of FSIs as a predictor (Fig. 3c, black bars, average RMSE of average FSI activity = 1.33 ± 0.24, $p = 0.003$, Dunnett's multiple comparison test).

If FSI ensembles encode speed, then a relationship should also exist with the derivative of speed: acceleration. Acceleration was predicted from FSI $\Delta F/F$ signals (Fig. 3d, $r = 0.68 \pm 0.06$, Fisher $z = 0.89 \pm 0.10$, $t = 9.20$, $n = 9$, $p < 0.0001$, one-sample t test). For all mice, compared to ensemble FSI activity, we observed a significantly greater RMSE in the GBM prediction of acceleration (Fig. 3e, red bars, average RMSE of composite of FSI activity = 1.87 ± 0.31, $F = 22.8$, $p = 0.001$, $n = 9$ mice, One-way RM ANOVA) as compared to using: (1) shuffled FSI data (Fig. 3e, light gray bars, average RMSE of randomized FSI activity = 2.92 ± 0.42, $p = 0.005$, Dunnett's multiple comparison test); (2) individual FSI data as a predictor and taking the mean of the resulting RMSEs (Fig. 3e, white bars, average RMSE of individual FSI activity = 2.95 ± 0.42, $p = 0.003$, Dunnett's multiple comparison test) or; (3) the average activity of FSIs as a predictor (Fig. 3e, black bars, average RMSE of average FSI activity = 2.99 ± 0.43, $p = 0.003$, Dunnett's multiple comparison test).

Discussion

Our data support the concept that FSIs functionally organize as ensembles that encode action speed of movement sub-components. Furthermore, our machine learning analyses suggest that this ensemble activation of FSIs is necessary for optimal encoding of action speed. The temporal coordination of FSIs as ensembles observed herein may resolve a recent in vivo electrophysiological study that suggests FSIs synchronize (Bakhurin et al. 2016) with other data suggesting that putative FSIs fire idiosyncratically associated with movement and action execution (Berke 2008). As a possible further explanation for discrepancies in the literature, our observation that FSI–FSI cross correlations exhibit a broad peak of correlated activity over time suggests that FSIs may coordinate firing (within ensembles) on a mesoscale, rather than with the high temporal precision that is usually associated with neural synchrony using electrophysiological approaches. Accordingly, it should be noted that Ca^{2+} imaging is a poor proxy for the high temporal dynamics of FSIs. Further work is required to determine if FSIs synchronize as ensembles on a millisecond timescale.

FSIs predominate in the dorsolateral striatum (Schlösser et al. 1999; Luk and Sadikot 2001), which receives primarily somatomotor cortical input (DeLong and Georgopoulos 1981; Lovinger 2010). As such, the present data suggest that FSI encoding of movement speed is communicated from motor cortical inputs. Given our observation that distinct FSI ensembles encode movement sub-component speed, an input specificity from motor cortex to FSI ensembles may exist. The segregation of FSI ensembles into distinct motor components may give rise to a scenario wherein ensembles encoding opposing or non-overlapping movement sub-components (e.g., arm flexure and extension) would exhibit non-overlapping activation patterns. Mice tend not to perform overt head scanning while ambulating and vice versa. This may explain negative correlations between a proportion of ambulation encoding FSIs and head movements and vice versa. It should finally be noted that our mouse movement tracking system is not able to detect all movement sub-components, such as whisking. Based on our observation that distinct ensembles encode movement sub-components, it is possible that the so-called stochastic FSIs may be encoding the speed of such undetected movements.

Synthesizing extant single-unit recording data showing that putative FSIs maintain a baseline level of firing (Lee et al. 2017; Wiltschko et al. 2010; Berke 2008; Bakhurin et al. 2016; Gage et al. 2010) with the present findings suggests that FSIs may provide sustained inhibitory governance, as ensembles, over MSN output that dynamically

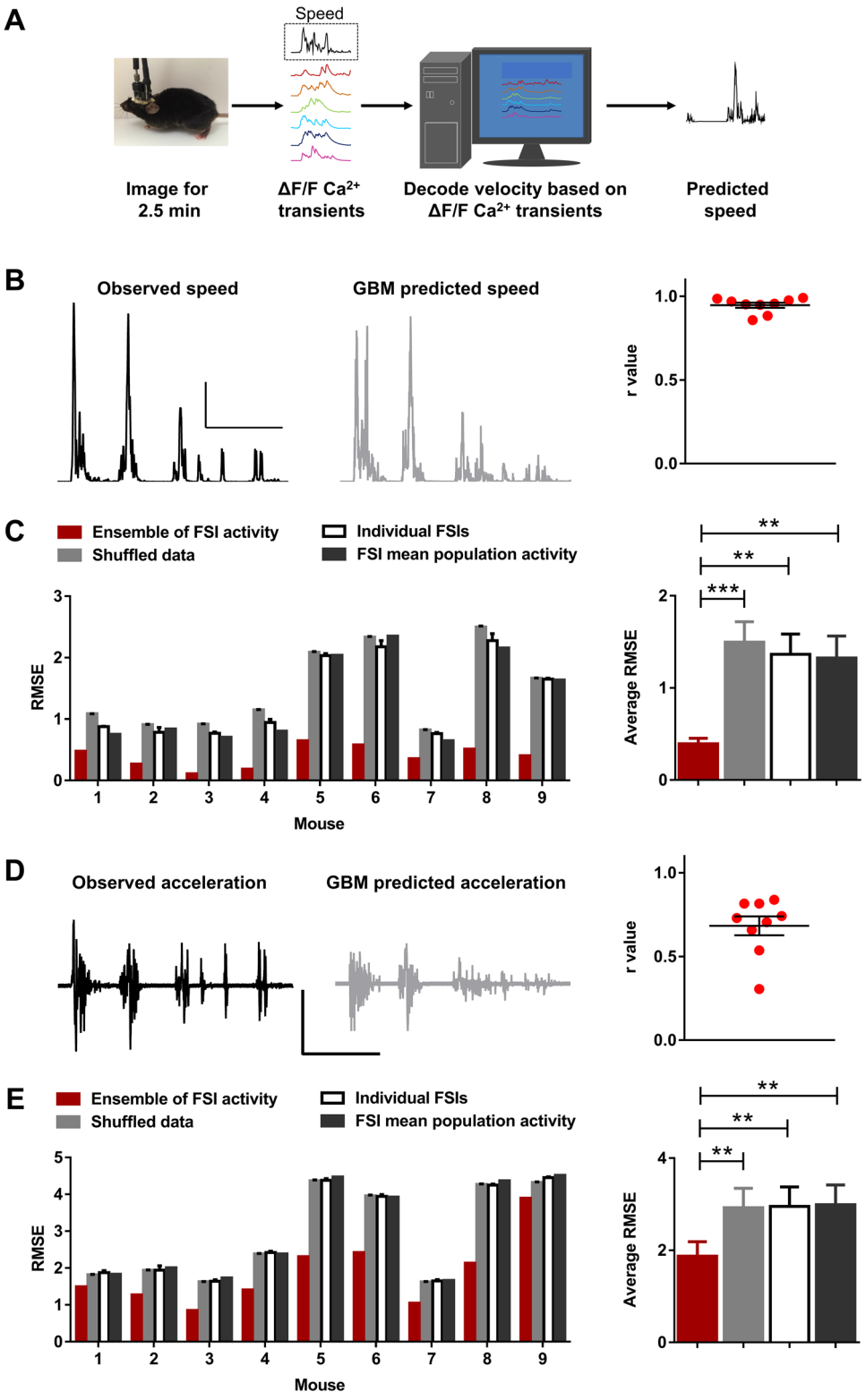

increases in a coordinated manner with movement speed. This view is not incompatible with previous electrophysiological recordings of FSIs during performance of a learned action sequence (Jin et al. 2014). In addition, despite the strength of Ca^{2+} imaging to detect genetically identified FSIs, this approach is limited in ability to detect baseline firing and therefore the possible coordination of FSIs during this state, which would coincide with inaction based

◂**Fig. 3** FSI population activity accurately predicts action speed. **a** Schematic of the workflow for applying a generalized boosted model (GBM) machine learning algorithm to predict movement using in vivo Ca2+imaging data. **b**. Left: representative traces are shown of observed speed (black trace) and GBM predicted speed (gray trace). Right: dot plot of the correlation between observed and predicted speed for each animal. Scale bars: 2 cm/s, 500 s. **c** Left: root mean square error (RMSE) magnitude is plotted for each mouse for the GBM predicting speed using Ca2+imaging data from FSI ensembles as predictors (red bars); using shuffled data of all FSIs as predictors (10 different permutations, gray bars); performing the GBM with each FSI individually as a predictor and taking the mean of the resulting RMSEs (white bars); and using the mean activity of all FSIs as the sole predictor (dark gray bars). Right: mean RMSE across animals for the four different GBM analyses shown on the left. One-way ANOVA revealed significantly less error between the observed and predicted speed for the GBM using all FSIs as predictors compared to the shuffled, individual, and mean FSI activity models. ***$p < 0.001$, **$p < 0.01$. **d** Left: representative traces are shown of observed acceleration (black trace) and GBM predicted acceleration (gray trace). Right: dot plot of the correlation between observed and predicted acceleration for each animal. Scale bars: 10 cm/s2, 500 s. **e** Left: RMSE is plotted for each mouse for the GBM predicting acceleration using Ca2+imaging data from FSI ensembles as predictors (red bars); using shuffled data of all FSIs as predictors (10 different permutations, gray bars); performing the GBM with each FSI individually as a predictor and taking the mean of the resulting RMSEs (white bars); and using the mean activity of all FSIs as the sole predictor (dark gray bars). Right: mean RMSE across animals for the four different GBM analyses shown on the left. One-way ANOVA revealed significantly less error between the observed and predicted acceleration for the GBM using all FSIs as predictors compared to the shuffled, individual, and mean FSI activity models. **$p < 0.01$

on our findings. Finally, while the study by Jin et al. (2014) and the present study focus on FSI encoding of movement, FSI encoding of somatosensation alone or in conjunction with movement speed cannot be ruled out.

FSIs are linked to habit formation (O'Hare et al. 2017). Therefore, it is worth investigating if/how dorsolateral striatal FSIs form ensembles during complex action sequences that are specific to dorsolateral striatal function. Given the postmortem data linking FSI dysfunction to movement disorders (Kalanithi et al. 2005; Kataoka et al. 2010; Reiner et al. 2013) and targeting of FSIs by drugs of abuse (Wiltschko et al. 2010; Blomeley et al. 2011; Patton et al. 2016, 2019), FSI ensemble encoding is positioned as a novel metric for dorsolateral striatal performance that may be disrupted in a variety of neuropsychiatric disorders.

Author contributions BMR, MGW, RC and BNM: designed the experiments. BMR: performed in vivo calcium imaging experiments. BMR and MGW: analyzed in vivo calcium imaging data. MGW and BMR: performed and analyzed electrophysiological experiments. RC: performed machine learning and simulation analyses. BMR, MGW, MHP, RC, and BNM: wrote the manuscript.

Compliance with ethical standards

Conflict of interest The authors declare no financial and non-financial competing interests. All applicable international, national, and/or institutional guidelines for the care and use of animals were followed. All procedures performed in studies involving animals were in accordance with the ethical standards of the institution or practice at which the studies were conducted. This work was supported by: National Institute on Alcohol Abuse and Alcoholism grants K22AA021414, R01AA024845 (B.N.M.) and F31AA024683 (M.H.P.); National Institute of General Medical Sciences grant T32008181 (M.G.W.); National Institute of Neurological Disorders and Stroke grant T32NS063391 (M.G.W.); National Institute of Neurological Disorders and Stroke and Brain Initiative grant R01NS110421 (R.C.); and National Institute of Mental Health grant F31MH112350 (M.G.W.).

References

Bakhurin KI, Mac V, Golshani P, Masmanidis SC (2016) Temporal correlations among functionally specialized striatal neural ensembles in reward-conditioned mice. J Neurophysiol 115:1521–1532. https://doi.org/10.1152/jn.01037.2015

Barbera G, Liang B, Zhang L, Gerfen CR et al (2016) Spatially compact neural clusters in the dorsal striatum encode locomotion relevant information. Neuron 92:202–213. https://doi.org/10.1016/j.neuron.2016.08.037

Barnes TD, Mao JB, Hu D, Kubota Y et al (2011) Advance cueing produces enhanced action-boundary patterns of spike activity in the sensorimotor striatum. J Neurophysiol 105:1861–1878. https://doi.org/10.1152/jn.00871.2010

Berke JD (2008) Uncoordinated firing rate changes of striatal fast-spiking interneurons during behavioral task performance. J Neurosci 28:10075–10080. https://doi.org/10.1523/JNEUROSCI.2192-08.2008

Blomeley CP, Cains S, Smith R, Bracci E (2011) Ethanol affects striatal interneurons directly and projection neurons through a reduction in cholinergic tone. Neuropsychopharmacology 36:1033–1046. https://doi.org/10.1038/npp.2010.241

DeLong MR, Georgopoulos AP (1981) Motor functions of the basal ganglia. In: Brookhart JM, Mountcastle VB, Brooks VB, Geiger SR (eds) Handbook of physiology. Sect. 1: The nervous system, vol II: Motor control. American Physiological Society, Bethesda, pp 1017–1061

Duda RO, Hart PE, Stork DG (2001) Pattern classification. Wiley, New York

Friedman J (2001) Greedy function approximation: a gradient boosting machine. Ann Stat 29:1189–1232

Friedman J (2002) Stochastic gradient boosting. Comput Stat Data Anal 38:367–378

Gage GJ, Stoetzner CR, Wiltschko AB, Berke JD (2010) Selective activation of striatal fast-spiking interneurons during choice execution. Neuron 67:466–479. https://doi.org/10.1016/j.neuron.2010.06.034

Graybiel AM (1998) The basal ganglia and chunking of action repertoires. Neurobiol Learn Mem 70:119–136

Guizar-Sicairos M, Thurman ST, Fienup JR (2008) Efficient subpixel image registration algorithms. Opt Lett 33:156–158

Hjorth J, Blackwell KT, Kotaleski JH (2009) Gap junctions between striatal fast-spiking interneurons regulate spiking activity and synchronization as a function of cortical activity. J Neurosci 29:5276–5286. https://doi.org/10.1523/JNEUROSCI.6031-08.2009

Jin X, Costa RM (2010) Start/stop signals emerge in nigrostriatal circuits during sequence learning. Nature 466:457–462. https://doi.org/10.1038/nature09263

Jin X, Tecuapetla F, Costa RM (2014) Basal ganglia subcircuits distinctively encode the parsing and concatenation of action sequences. Nat Neurosci 17:423–430

Kalanithi PS, Zheng W, Kataoka Y, DiFiglia M et al (2005) Altered parvalbumin-positive neuron distribution in basal ganglia of individuals with Tourette syndrome. Proc Natl Acad Sci USA 102:13307–13312

Kataoka Y, Kalanithi PS, Grantz H, Schwartz ML et al (2010) Decreased number of parvalbumin and cholinergic interneurons in the striatum of individuals with Tourette syndrome. J Comp Neurol 518:277–291. https://doi.org/10.1002/cne.22206

Klaus A, Martins GJ, Paixao VB, Zhou P et al (2017) The spatiotemporal organization of the striatum encodes action space. Neuron 95:1171–1180. https://doi.org/10.1016/j.neuron.2017.08.015

Koos T, Tepper JM, Wilson CJ (2004) Comparison of IPSCs evoked by spiny and fast-spiking neurons in the neostriatum. J Neurosci 24(36):7916–7922

Kuhn M (2008) Building predictive models in R using the caret package. J Stat Softw 28:1–26

Lee K, Holley SM, Shobe JL, Chong NC et al (2017) Parvalbumin interneurons modulate striatal output and enhance performance during associative learning. Neuron 93:1451–1463. https://doi.org/10.1016/j.neuron.2017.02.033

London TD, Licholai JA, Szczot I, Ali MA et al (2018) Coordinated ramping of dorsal striatal pathways preceding food approach and consumption. J Neurosci 38(14):3547–3558. https://doi.org/10.1523/JNEUROSCI.2693-17.2018

Lovinger DM (2010) Neurotransmitter roles in synaptic modulation, plasticity and learning in the dorsal striatum. Neuropharmacology 58(7):951–961

Luk KC, Sadikot AF (2001) GABA promotes survival but not proliferation of parvalbumin-immunoreactive interneurons in rodent neostriatum: an in vivo study with stereology. Neuroscience 104:93–103

Mathur BN, Tanahira C, Tamamaki N, Lovinger DM (2013) Voltage drives diverse endocannabinoid signals to mediate striatal microcircuit-specific plasticity. Nat Neurosci 16:1275–1283

O'Hare JK, Li H, Kim N, Gaidis E et al (2017) Striatal fast-spiking interneurons selectively modulate circuit output and are required for habitual behavior. Elife. 6:e26231. https://doi.org/10.7554/eLife.26231

Owen SF, Berke JD, Kreitzer AC (2018) Fast-spiking interneurons supply feedforward control of bursting, calcium, and plasticity for efficient learning. Cell 172:683–695.e15. https://doi.org/10.1016/j.cell.2018.01.005

Patton MH, Roberts BM, Lovinger DM, Mathur BN (2016) Ethanol disinhibits dorsolateral striatal medium spiny neurons through activation of a presynaptic delta opioid receptor. Neuropsychopharmacology 41:1831–1840. https://doi.org/10.1038/npp.2015.353

Patton MH, Padgett KE, McKeon PN, Lu SG et al (2019) An Aplysia-like synaptic switch for rapid protection against ethanol-induced synaptic inhibition in a mammalian habit circuit. Neuropharmacology 144:1–8. https://doi.org/10.1016/j.neuropharm.2018.10.010

Pnevmatikakis EA, Soudry D, Gao Y, Machado TA et al (2016) Simultaneous denoising, deconvolution, and demixing of calcium imaging data. Neuron 89:285–299. https://doi.org/10.1016/j.neuron.2015.11.037

Reiner A, Shelby E, Wang H, Demarch Z et al (2013) Striatal parvalbuminergic neurons are lost in Huntington's disease: implications for dystonia. Mov Disord 28:1691–1699. https://doi.org/10.1002/mds.25624

Schlösser B, Klausa G, Prime G, Ten Bruggencate G (1999) Postnatal development of calretinin- and parvalbumin-positive interneurons in the rat neostriatum: an immunohistochemical study. J Comp Neurol 405:185–198

Tanahira C, Higo S, Watanabe K, Tomioka R et al (2009) Parvalbumin neurons in the forebrain as revealed by parvalbumin-Cre transgenic mice. Neurosci Res 63:213–223. https://doi.org/10.1016/j.neures.2008.12.007

Tepper JM, Koós T, Wilson CJ (2004) GABAergic microcircuits in the neostriatum. Trends Neurosci 27:662–669

Tepper JM, Tecuapetla F, Koós T, Ibáñez-Sandoval O (2010) Heterogeneity and diversity of striatal GABAergic interneurons. Front Neuroanat 4:150

White MG, Cody PA, Bubser M, Wang HD et al (2017) Cortical hierarchy governs rat claustrocortical circuit organization. J Comp Neurol 525:1347–1362. https://doi.org/10.1002/cne.23970

Wiltschko AB, Pettibone JR, Berke JD (2010) Opposite effects of stimulant and antipsychotic drugs on striatal fast-spiking interneurons. Neuropsychopharmacology 35:1261–1270. https://doi.org/10.1038/npp.2009.226

Yttri EA, Dudman JT (2016) Opponent and bidirectional control of movement speed in the basal ganglia. Nature 533:402–406. https://doi.org/10.1038/nature17639

Zhang M, Zhao Z, He P, Wang J (2014) Effect of gap junctions on the firing patterns and synchrony for different external inputs in the striatal fast-spiking neuron network. Biomed Mater Eng 24:2635–2644. https://doi.org/10.3233/BME-141080